Coupling cobalt sulfide nanosheets with cadmium sulfide nanoparticles for highly efficient visible-light-driven photocatalysis

Fan Zhang[a], Hua-Qiang Zhuang[b], Jie Song[c], Yu-Long Men[a], Yun-Xiang Pan[a,*], Shu-Hong Yu[d,*]

[a] Anhui Province Key Laboratory of Advanced Catalytic Materials and Reaction Engineering, School of Chemistry and Chemical Engineering, Hefei University of Technology, Hefei 230009, PR China
[b] College of Chemical Engineering and Materials Science, Quanzhou Normal University, Quanzhou 362000, Fujian Province, PR China
[c] Institute of Nano Biomedicine and Engineering, Department of Instrument Science and Engineering, School of Electronic Information and Electrical Engineering, Shanghai Jiao Tong University, No. 800, Dongchuan Road, Shanghai 200240, PR China
[d] Division of Nanomaterials & Chemistry, Hefei National Laboratory for Physical Sciences at Microscale, Department of Chemistry, University of Science and Technology of China, Hefei 230026, PR China

ARTICLE INFO

ABSTRACT

Developing noble-metal-free photocatalysts highly flexible for separating the photogenerated electron-hole pairs is crucial for the solar-energy-driven photocatalysis, but still remains an open question. Herein, we fabricated two dimensional Co_3S_4 nanosheets with a thickness of about 10 nm, and applied the nanosheets to support CdS nanoparticles (~5 nm) to form a noble-metal-free CdS/Co_3S_4 photocatalyst with a higher ability in charge separation. In the visible-light-driven photocatalytic H_2O splitting, an enhanced H_2 evolution (1083.9 μmol h^{-1}) was achieved on CdS/Co_3S_4, as compared with those on the CdS-nanoparticle-loaded Co_3S_4 nanoparticles (775.5 μmol h^{-1}) and noble-metal-based CdS/Pt photocatalyst (566.3 μmol h^{-1}). The enhanced photocatalytic performance is the result of the multiple roles of the Co_3S_4 nanosheets in the photocatalytic reaction, including promoting electron-hole separation, providing catalytically active sites and suppressing the aggregation of the CdS nanoparticles responsible for light absorption.

1. Introduction

Solar-energy-driven photocatalysis, such as photocatalytic H_2O splitting and photocatalytic reduction of CO_2, is a promising renewable energy technology [1,2]. The ability of the photocatalysts in separating the photogenerated electron-hole pairs is a key factor affecting the photocatalytic efficiency [3–8]. Developing photocatalysts highly flexible for electron-hole separation is thereby a hot topic in chemistry.

Two-dimensional (2D) materials are of particularly interest for photocatalysis [9–18]. The transfer of the photogenerated charge carriers from the interior to the surface active sites and along the in-plane surface in 2D materials are easier, due to the smaller resistances, shortened transport distances and quantum confinement effects in the two dimensions, as compared with the bulk materials [9–11]. This makes the 2D materials highly flexible for separating the photogenerated electron-hole pairs. Besides, 2D materials have more surface defects and low-coordinated atoms, which are catalytically active sites, than the bulk materials [12,13]. These advantages make the 2D materials highly efficient for photocatalysis. For example, the photocatalytic CO_2 reduction efficiency on $SrNb_2O_6$ nanoplates is higher than those on

$SrNb_2O_6$ nanoparticles and $SrNb_2O_6$ nanorods, due to the more efficient electron-hole separation and abundant active sites on $SrNb_2O_6$ nanoplates [14]. Another example, the improved electron-hole separation due to the shorter electrons/holes transfer distances makes the CO and CH_4 evolution rates in the photocatalytic CO_2 reduction on BiOI nanosheets higher than that on the bulk BiOI [15].

The noble-metal-free cobalt sulfide (Co_xS_y) has been widely explored for substituting the rare and expensive noble metals, e.g. Pt, to fabricate photocatalysts [19–23]. Yu et al. found that cobalt sulfide quantum dots (QDs) can effectively accelerate the photogenerated electron-hole separation, promote the electron transfer to catalytically active sites and serve as the active site for the photocatalytic reactions, resulting in a H_2 production rate of 41.9 μmol h^{-1}, in the photocatalytic H_2O splitting [19]. Zheng et al. observed a H_2 evolution rate of 5.98 μmol h^{-1} in the photocatalytic H_2O splitting on a cobalt sulfide photocatalyst, with triethanolamine and Eosin-Y as sacrificial electron donor and photosensitizer, respectively [20]. Hollow cobalt sulfide cubes embedded with cadmium sulfide (CdS) QDs were reported to be highly active for light harvesting due to the multiple reflections of light in the cubic structure, and for the photogenerated electron-hole

* Corresponding authors.
E-mail addresses: tjupyx@hfut.edu.cn (Y.-X. Pan), shyu@ustc.edu.cn (S.-H. Yu).

separation due to the intimate interface between the cubes and QDs, leading to a H_2 evolution rate of 21.2 μmol h^{-1} from the photocatalytic H_2O splitting [21]. Despite the extensive explorations, the photocatalytic efficiency of cobalt-sulfide-based photocatalysts is still too low, and requires further improvement.

Herein, we fabricated 2D Co_3S_4 nanosheets with a thickness of about 10 nm, and loaded CdS nanoparticles (~5 nm) on the nanosheets to form a noble-metal-free CdS/Co_3S_4 photocatalyst. In the photocatalytic H_2 evolution from H_2O under the irradiation of visible light which is the main part of sunlight (44%), CdS/Co_3S_4 shows a H_2 evolution rate of 1083.9 μmol h^{-1}, which is higher than those on the CdS-nanoparticle-loaded Co_3S_4 nanoparticles (775.5 μmol h^{-1}) and noble-metal-based CdS/Pt photocatalyst (566.3 μmol h^{-1}). In the photocatalytic reactions, the Co_3S_4 nanosheets promote the electron-hole separation, provide catalytically active sites, suppress the aggregation of the CdS nanoparticles which act as light absorbers, thus enhancing the photocatalytic performance.

2. Experimental

2.1. Sample preparation

The reagents used in the experiments, including cobalt acetate tetrahydrate ($C_4H_6CoO_4 \cdot 4H_2O$), thiourea, hydrazine hydrate, diethylenetriamine (DETA), chloroplatinic acid hexahydrate ($H_2PtCl_6 \cdot 6H_2O$), were all in analytical grade purity, and were commercially obtained from Alfa Aesar. The CdS nanoparticles were prepared by using a hot-inject method which has been described detailedly in the previous works [24–28].

For fabricating the Co_3S_4 nanosheets, 1 mmol of cobalt acetate tetrahydrate and 0.5 mmol of thiourea were firstly dispersed in a mixture containing hydrazine hydrate (4 mL) and DETA (36 mL) under stirring. And then, the solution was transferred into a 50 mL Teflon-lined stainless autoclave. Next, the solution in the autoclave was kept at 180 °C for 24 h, followed by cooling to room temperature naturally. The hydrothermal-synthesized sample was then centrifuged, and washed by deionized (DI) water and ethanol for several times. After washing, the precipitate was dried under vacuum at 25 °C for 12 h, leading to the formation of the Co_3S_4 nanosheets.

The procedure for preparing the Co_3S_4 nanoparticles is similar to that of the Co_3S_4 nanosheets, except that DI water (36 mL) was used to dissolve the cobalt acetate tetrahydrate, thiourea and hydrazine hydrate for the hydrothermal process, instead of DETA. Co_3O_4 was obtained through calcination on the Co_3S_4 nanosheets at 500 °C for 2 h under air atmosphere.

For loading the CdS nanoparticles on the Co_3S_4 nanosheets to form CdS/Co_3S_4, 20 mg of the Co_3S_4 nanosheets were dispersed in 10 mL of water solution containing 40 mg of the hydrophobic CdS nanoparticles under ultrasonication for 2 h at room temperature. The mixed solution was centrifuged to collect the solid sample, which was washed by DI water and ethanol for several times and dried under vacuum at 25 °C for 12 h, leading to the formation of CdS/Co_3S_4. The procedures for loading CdS nanoparticles on the Co_3S_4 nanoparticles and Co_3O_4 to fabricate CdS/Co_3S_4(P) and CdS/Co_3O_4 are the same as that for CdS/Co_3S_4. Combination of the commercial CdS (Sigma–Aldrich, purity: 99.999%) with the Co_3S_4 nanosheets to produce $CdS(C)/Co_3S_4$ also proceeded through the procedure same as that of CdS/Co_3S_4.

The procedure for preparing CdS/Pt was as follows. 0.53 mg of $H_2PtCl_6 \cdot 6H_2O$ containing 0.20 mg of Pt was dispersed in 10 mL of water solution containing 40 mg of hydrophobic CdS nanoparticles under ultrasonication for 2 h at room temperature, combining Pt ions with the CdS nanoparticles together. Then, the sample was irradiated for 2 h by using a 300 W Xe-lamp under stirring, reducing Pt ions into Pt^0. Finally, the solid sample was harvested by centrifugation, washed with ethanol and DI water for several times, and dried under vacuum at 25 °C for 12 h, fabricating CdS/Pt.
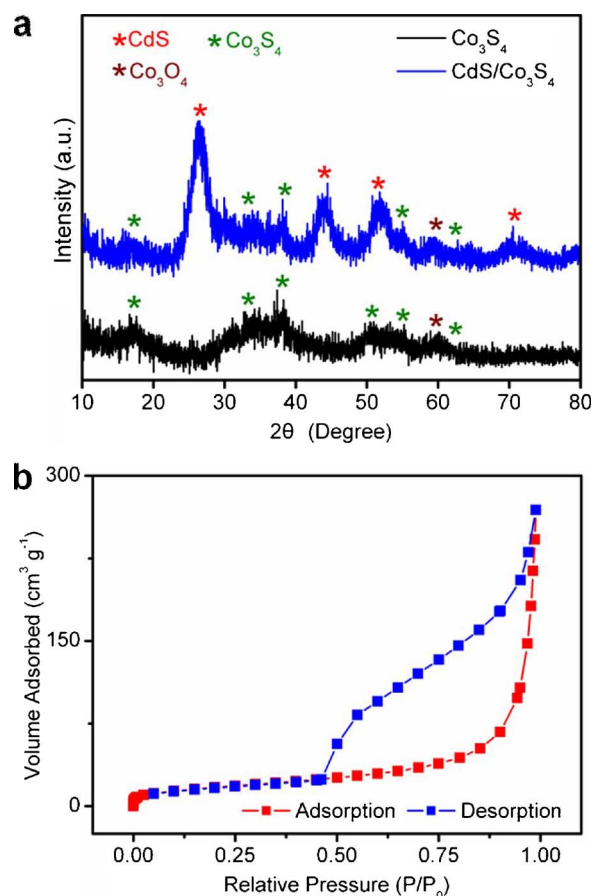

Fig. 1. XRD patterns of the pure Co_3S_4 nanosheets and CdS/Co_3S_4 (a). N_2 adsorption-desorption isotherm of the pure Co_3S_4 nanosheets (b).

2.2. Characterization

The crystalline structure of the samples were analyzed by X-ray diffraction (XRD) patterns using an X-ray diffractometer (Bruker AXS D8, Cu Kα, λ = 1.5406 Å, 40 kV and 40 mA). The scanning electron microscopy (SEM) images were obtained on a Sirion200 field emission scanning electron microscope. A Multimode SPM (Veeco Instruments) operated in the tapping mode and with silicon cantilevers (typical spring constant: 30 N m^{-1}, resonant frequency: 240 kHz) was used for the atomic force microscopy (AFM) observations. About 10 L aliquots of the samples were deposited on a freshly cleaved mica surface, followed by air-dried and imaged using AFM. The Brunauer-Emmett-Teller (BET) surface areas of the samples were observed through N_2 absorption-desorption experiments on a Micromeritics Tristar II 3020 M apparatus. The X-ray photoelectron spectroscopy (XPS) spectra were obtained on an ESCALAB250Xi X-ray photoelectron spectrophotometer (Al Kα) with a Thermo-manufactured monochromatized radiation as the X-ray source. The photoluminescence (PL) spectra were measured on a JY Fluorolog 3-TAU luminescence spectrometer (Jobin Yvon Instruments Co., Ltd., France), with an excitation wavelength of 365 nm. The transmission electron microscope (TEM) observations, including high resolution TEM (HRTEM) and elemental mapping, were preformed on a JEOL JEM 2100F with a beam energy of 200 kV. The UV–visible spectra were investigated on a UV-2450 UV–vis spectrophotometer (Shimadzu). A ZetaPALS Zeta Potential Analyzer (Brookhaven Instruments Corporation) was applied for observing the Zeta potentials of the samples.

The transient photocurrents response of the samples were measured on a CHI660A electrochemical workstation in a Na_2SO_4 solution (0.2 M) containing lactic acid (10 vol%) which was used as a hole
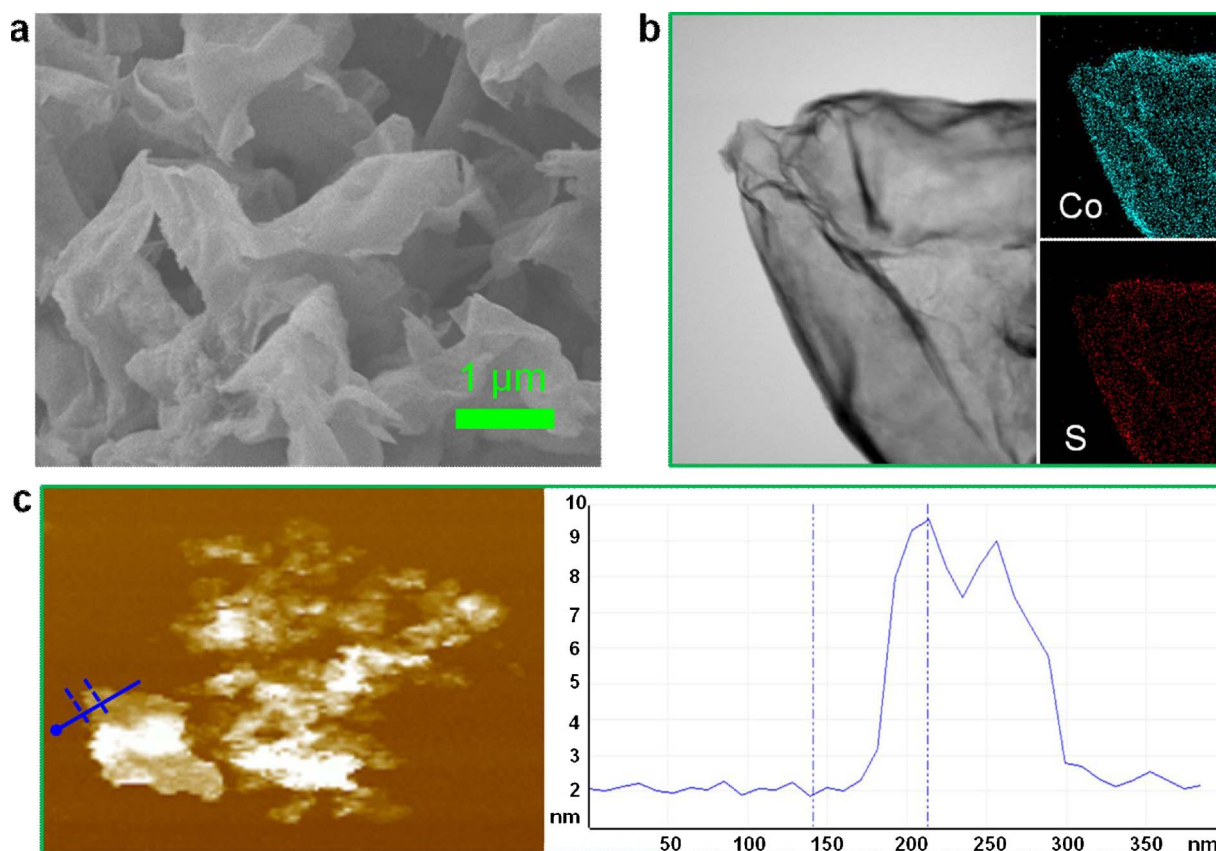
Fig. 2. SEM image (a), TEM image and elemental mapping patterns (b), and AFM image (left panel) with the height profile (right panel) (c) for the pure Co$_3$S$_4$ nanosheets.

scavenger during the photocatalytic reactions, with a constant potential of 0.35 V *vs.* standard electrode. The solution and light source (300 W Xe-lamp with a cut-off filter λ > 420 nm) used for measuring the photocurrents were similar to those for the photocatalytic reactions. The electrochemical workstation includes three electrodes. A Pt plate and a saturated calomel electrode were the counter electrode and reference electrode, respectively. The working electrode was formed by coating the sample on a glassy carbon electrode (GCE), with a surface area of 0.07 cm^2 exposed to the electrolyte. For coating the sample on the GCE, 1 mg of sample was firstly dispersed in ethanol (1 mL) containing 0.05 wt% naphthol under ultrasonication to form a suspension. Then, the suspension was deposited onto the GCE, and dried at room temperature for 30 min. The electrochemical impedance spectra of the samples were obtained by using a three-electrode system, including a working electrode with the sample, a reference electrode with KCl-saturated Ag/AgCl and a counter electrode with a Pt plate, in a frequency range from 0.1 Hz to 100 kHz with a AC voltage amplitude of 5.0 mV, at room temperature on the CHI660A electrochemical workstation.

2.3. Visible-light-driven photocatalytic H$_2$O splitting

The visible-light-driven photocatalytic H$_2$O splitting was performed in a closed gas circulation vacuum system equipped with a Pyrex cell. The volume of the photoreactor was 300 mL. A 300 W Xe-lamp with a cutoff filter (λ > 420 nm) was used as the visible light source. During the photocatalytic reactions, the lamp power remained constant, and the distance between the reactor and the lamp was fixed at about 10 cm. In the photoreactor, the photocatalyst (100 mg) was dispersed in a water solution (100 mL) containing 10 vol% lactic acid as a hole scavenger. Before opening the lamp, the reaction system was evacuated and refilled with argon for several times to remove the air inside. During the photocatalytic reactions, the temperature of the reaction system was kept at about 20 °C by using cooling water. The H$_2$ evolved

was detected by an online gas chromatography (Agilent 7890A, Thermal Conductivity Detector). The QE was measured under the conditions same as the photocatalytic reactions with band-pass with center wavelength at 420, 440, 460, 480, 500, and 520 nm, respectively. A silicon photodiode (13 DAS 005, MELLES GRIOT) connected to a broad-band power/energy meter (13 PEM001, MELLES GRIOT) was used to measure the number of incident photons. The QE was calculated by using Eq. (1):

$$QE = \frac{2 \times (\text{the number of H}_2\text{molecules produced})}{\text{the number of incident photons}} \times 100\% \tag{1}$$

3. Results and discussion

3.1. Co$_3$S$_4$ nanosheets

Fig. 1a shows the XRD pattern of the cobalt sulfide sample synthesized by hydrothermal process. The peaks at 16.1, 31.4, 38.0, 50.2, 55.0 and 62.2° on the XRD patterns are attributed to the linnaeite Co$_3$S$_4$ (JCPDS No. 42-1448). As such, the cobalt sulfide hydrothermal-synthesized herein is linnaeite Co$_3$S$_4$. On the XRD pattern, besides the peaks of Co$_3$S$_4$, there is also a peak locating at 59.4°, which may be caused by Co$_3$O$_4$ (JCPDS No. 42-1467). It has been reported that cobalt sulfide can be contaminated with cobalt oxide when it is exposed to air [19–23]. It is thereby reasonable to observe Co$_3$O$_4$ on the sample. Through N$_2$ adsorption-desorption experiments (Fig. 1b), the BET surface area of the hydrothermal-synthesized Co$_3$S$_4$ was measured to be 62.8 m^2 g^{-1}. As reflected by SEM (Fig. 2a), TEM (Fig. 2b) and AFM images (Fig. 2c), the hydrothermal-synthesized Co$_3$S$_4$ are 2D nanosheets, with a thickness of about 10 nm (Fig. 2c). Elemental mapping patterns confirm the presence of Co and S on the Co$_3$S$_4$ nanosheets (Fig. 2b).

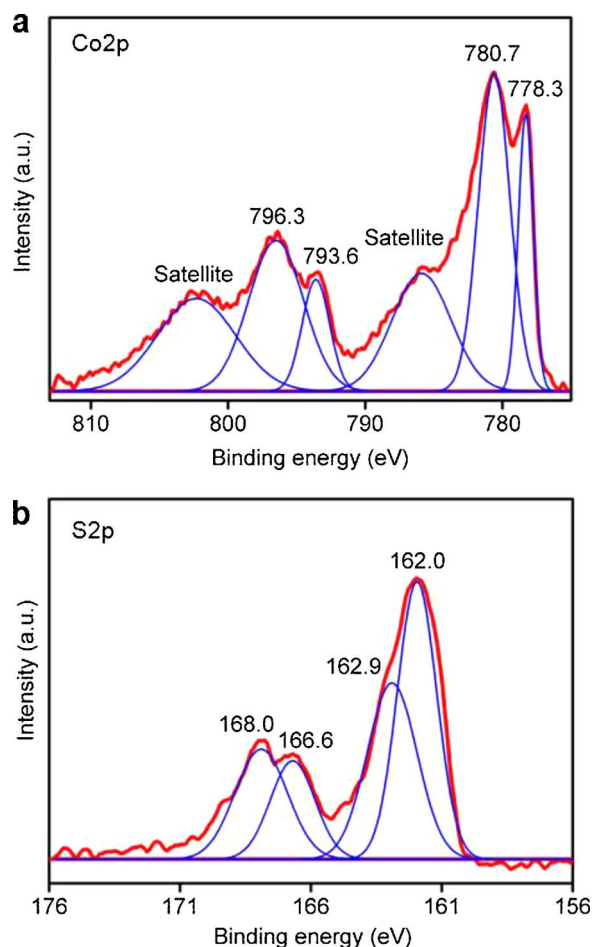We further characterized the Co$_3$S$_4$ nanosheets by using XPS spectra

Fig. 3. XPS spectra of Co2p (a) and S2p (b) for the pure Co_3S_4 nanosheets.

Fig. 4. TEM (a) and HRTEM (b) images of the coupled CdS/Co_3S_4 nanocomposite.

calibrated by the peak of C1s. The Co2p XPS spectrum of the Co_3S_4 nanosheets can be deconvoluted into peaks at 778.3, 780.7, 785.9, 793.6, 796.3 and 802.2 eV, respectively, as illustrated in Fig. 3a. The peaks at 778.3 and 793.6 eV could be due to the $2p_{3/2}$ and $2p_{1/2}$ of Co of Co_3S_4, respectively [29,30]. The peaks at 780.7 and 796.3 eV could be caused by the $2p_{3/2}$ and $2p_{1/2}$ of Co of cobalt oxide or cobalt oxy-sulfide formed on the surface of Co_3S_4 [29–31]. The broad peaks at 785.9 and 802.2 eV are satellite signals [29]. The XPS results imply the formation of the oxidized Co species on the surface of the Co_3S_4 na-nosheets. This is in good agreement with the XRD pattern (Fig. 1a). The S2p XPS spectrum of the Co_3S_4 nanosheets can be fitted into peaks at 162.0, 162.9, 166.8 and 168.0 eV, respectively (Fig. 3b). The peaks at 162.0 and 162.9 eV could be assigned to the $2p_{3/2}$ and $2p_{1/2}$ of S in Co_3S_4, respectively [29,30]. The peaks at 166.6 and 168.0 eV could be resulted from S in SO_3^{2-} and SO_4^{2-}, respectively [32,33].

3.2. Coupled CdS/Co_3S_4 nanocomposite

The CdS nanoparticles used for fabricating the CdS/Co_3S_4 nano-composite have been described previously [24–28]. A HRTEM ob-servation (Fig. S1a in the Supplementary Data) demonstrates that the CdS nanoparticles have a size of about 5 nm. In addition, the CdS na-noparticles are the standard cubic phase of CdS, as confirmed by the XRD pattern (JCPDS No. 10-0454, Fig. S1b). The CdS nanoparticle surface is coated by mercaptopropionic acid (MPA) molecule. The MPA molecule chain binds to the CdS nanoparticles *via* one of its two ends, *i.e.* thiol group. The other end of the MPA molecule chain, *i.e.* car-boxylic group, is deprotonated in water solution, making the CdS na-noparticles hydrophobic and negatively charged. The Zeta potential of
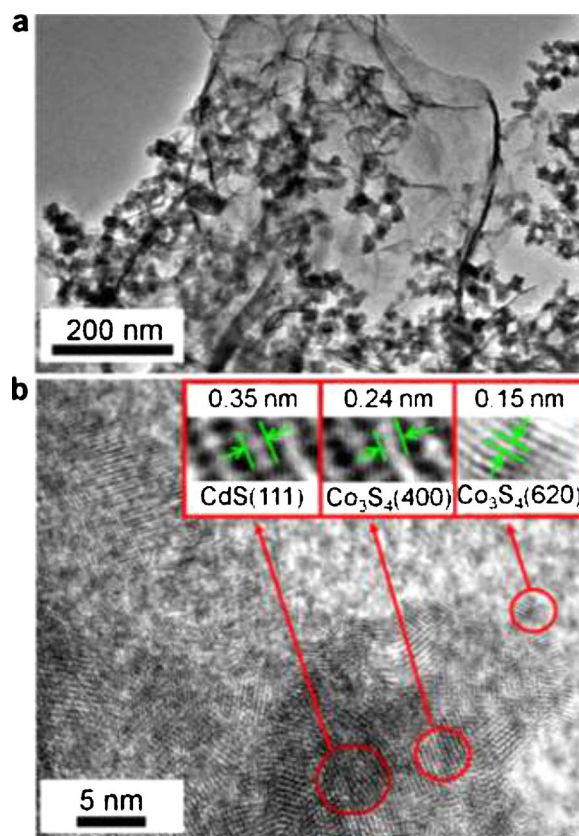
the pure CdS nanoparticles was measured to be -36.2 mV.

The XRD pattern of CdS/Co_3S_4 is plotted in Fig. 1a. In addition to the peaks attributed to Co_3S_4, the peaks caused by the standard cubic CdS are present at 26.5, 44.0, 52.1 and 70.4° (JCPDS No. 10-0454). Fig. 4 shows the TEM and HRTEM images of CdS/Co_3S_4. The CdS na-noparticles are dispersed on the Co_3S_4 nanosheets (Fig. 4a). The lattice fringes observed in the HRTEM image (Fig. 4b) with distances of 0.35, 0.25 and 0.15 nm are originated from CdS(111), Co_3S_4(400) and Co_3S_4(620) planes, respectively. The UV–vis spectra (Fig. S2 in the Supplementary Data) indicate that CdS/Co_3S_4 has a high ability in absorbing visible light, with an absorption edge at about 500 nm. This is similar to that of the pure CdS nanoparticles. The BET surface area of CdS/Co_3S_4 (74.1 $m^2 g^{-1}$) is slightly larger than that of the pure Co_3S_4 nanosheets. Loading of the CdS nanoparticles on the Co_3S_4 nanosheets could make the sample rougher, and thus enlarge the surface area of the sample. As compared with the pure Co_3S_4 nanosheets, the peaks on the XPS spectrum of Co2p on CdS/Co_3S_4 shift to higher binding energies (Fig. 5a). This may be originated from the interaction between CdS nanoparticles and Co_3S_4 nanosheets, possibly through the formation of the bonds between the Co atoms of Co_3S_4 and the S atoms of CdS [29–31]. Two peaks locating at 405.2 and 411.9 eV can be seen on the XPS spectrum of the Cd3d on CdS/Co_3S_4 (Fig. 5b), and be attributed to the $3d_{3/2}$ and $3d_{5/2}$ of the Cd atoms binding to the S atoms [34].

We next explore the capability of the CdS/Co_3S_4 nanocomposite in separating the photogenerated electron-hole pairs, which is a crucial factor affecting the photocatalytic performance, by using PL spectra and transient photocurrent response (Fig. 6). The pure CdS nanoparticles show a high PL peak at about 490 nm, which is caused by the photo-generated electron-hole recombination (Fig. 6a) [24–28]. After loading the CdS nanoparticles on the Co_3S_4 nanosheets, the PL peak at 490 nm disappears, implying a more efficient photogenerated electron-hole separation (Fig. 6a). The more efficient electron-hole separation on CdS/Co_3S_4 is also revealed by the much higher transient photocurrent
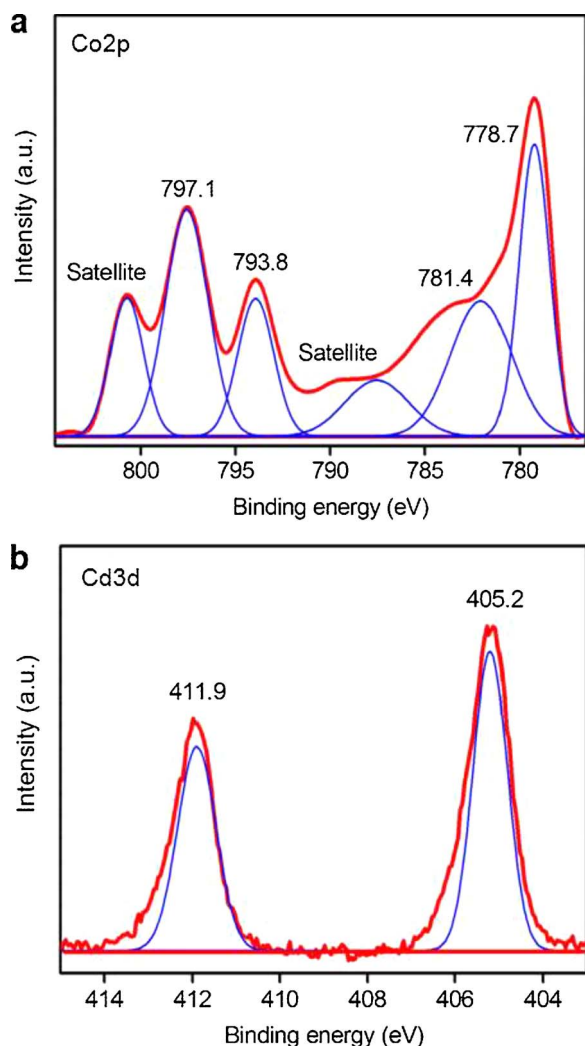
Fig. 5. XPS spectra of Co2p (a) and Cd3d (b) for the coupled CdS/Co₃S₄ nanocomposite.

response of CdS/Co₃S₄ than that of the pure CdS nanoparticles (Fig. 6b).

3.3. Visible-light-driven photocatalytic H_2 evolution from H_2O

As illustrated in Fig. 7a, during the visible-light-driven photocatalytic H_2 evolution from H_2O solution with lactic acid (10 vol%) as a hole scavenger, there is no H_2 detected on the pure Co_3S_4 nanosheets. The pure CdS nanoparticles are photocatalytically active, but exhibit a H_2 evolution rate of only 20.5 µmol h^{-1}. By varying the molar ratio of the cobalt acetate tetrahydrate to thiourea used in preparing the cobalt sulfides as well as the mass ratio of the CdS nanoparticles to the Co_3S_4 nanosheets for preparing CdS/Co₃S₄, an optimum H_2 evolution rate of 1083.9 µmol h^{-1} was achieved (Figs. S3 and S4 in the Supplementary Data). This is much higher than those on the pure CdS nanoparticles and the pure Co_3S_4 nanosheets (Fig. 7a). The photocatalytic activity of the noble-metal-based CdS/Pt photocatalyst was also explored. By changing the Pt content on CdS/Pt, an optimal H_2 evolution rate of 566.3 µmol h^{-1} was obtained (Fig. S5 in the Supplementary Data). The H_2 evolution rate on CdS/Co₃S₄ is about 2 times higher than that on CdS/Pt. Thus, the noble-metal-free Co_3S_4 nanosheets are good alternatives to the noble metal, i.e. Pt, to be used as cocatalysts providing active sites for the photocatalytic reactions.

Besides the pure CdS nanoparticles, the pure Co_3S_4 nanosheets and CdS/Pt, the photocatalytic activity of another three control samples were also studied for comparison. In the first control sample, the CdS nanoparticles were loaded on Co_3O_4. Co_3O_4 was fabricated by calcining

the Co_3S_4 nanosheets at 500 °C under air for 2 h. The second control sample was formed by loading the commercial CdS with an average particle size of approximately 200 nm (Fig. S6 in the Supplementary Data), denoted by CdS(C), on the Co_3S_4 nanosheets. The third control sample contains the CdS nanoparticles and the Co_3S_4 nanoparticles (Fig. S7 in the Supplementary Data), denoted by Co_3S_4(P). The methods used to load the CdS nanoparticles on Co_3O_4, combine CdS(C) with the Co_3S_4 nanosheets and combine the CdS nanoparticles with Co_3S_4(P) are the same as that for preparing CdS/Co₃S₄. For clarity, the three control samples are denoted by CdS/Co₃O₄, CdS(C)/Co₃S₄ and CdS/Co₃S₄(P), respectively. As plotted in Fig. 7a, the H_2 evolution rates on CdS/Co₃O₄, CdS(C)/Co₃S₄ and CdS/Co₃S₄(P) are 161.5, 131.0 and 775.5 µmol h^{-1}, respectively. These are all much lower than that on CdS/Co₃S₄. We also compared the efficiency of CdS/Co₃S₄ in producing H_2 with those of the photocatalysts reported previously [25,35–41]. As listed in Table S1 in the Supporting Informatio, as compared with the reported photocatalysts, the efficiency of CdS/Co₃S₄ in producing H_2 is higher or comparable.

The QE values of CdS/Co₃S₄ at wavelengths of 420, 440, 460, 480, 500 and 520 nm are plotted in Fig. 7b. Increasing the wavelength of the monochromatic light from 420 to 460 nm, the QE becomes higher, while with the wavelength larger than 460 nm, the QE decreases. The highest QE, with a value of 33.7%, was obtained at 460 nm. The CdS/Co₃S₄ has an enhanced stability in H_2 evolution, as compared with CdS/Pt (Fig. 8). The decrease of the total amount of H_2 produced after four runs on CdS/Co₃S₄ is only 4.1%, from 4335.6 µmol in the first run to 4157.8 µmol in the fourth run, whereas the decrease on CdS/Pt is 10.1%. As shown in Fig. S8 in the Supplementary Data, the XRD pattern of the CdS/Co₃S₄ after the photocatalytic stability examination shows the peaks attributed to Co_3S_4 and CdS, which is similar to that of the fresh CdS/Co₃S₄. Thus, there is no change in the valence state of the photocatalyst during the photocatalytic reaction.

3.4. Discussions

During the photocatalytic reactions, the hydrophobic CdS nanoparticles are responsible for the light absorption [24–28]. As such, the zero H_2 evolution on the pure Co_3S_4 nanosheets is originated from the absence of the light absorber. The hydrophobic CdS nanoparticles are used as the light absorber due to the following advantages. Firstly, the nanoscale CdS nanoparticles have been shown to have a quantum size-confinement effect, which is favorable for light absorption and photogenerated electron-hole separation [26]. Secondly, the hydrophobic CdS nanoparticles could result in better interactions of the photocatalyst with the H_2O molecules. This is benefit for enhancing the conversion of H_2O into H_2. Thirdly, a good dispersion of the CdS nanoparticles and the resulting favorable interaction with the Co_3S_4 nanosheets could also be important towards an improved photocatalytic performance [24]. These advantages could be responsible for the higher H_2 evolution rate on CdS/Co₃S₄ than that on CdS(C)/Co₃S₄ (Fig. 7a).

The role of the Co_3S_4 nanosheets during the photocatalytic reactions is multiple. Firstly, the Co_3S_4 nanosheets enhance the separation of the photogenerated electron-hole pairs formed on the CdS nanoparticles, and promote the transfer of the electrons from the CdS nanoparticles to the catalytically active sites. The enhanced electron-hole separation in the presence of the Co_3S_4 nanosheets may be due to the smaller resistances, shortened transport distances and strong quantum confinement effects in the two dimensions of the Co_3S_4 nanosheets [11–16]. We compared the electron-hole separation efficiency on the photocatalyst using the Co_3S_4 nanosheets with that using Co_3S_4(P), i.e. Co_3S_4 nanoparticles, by measuring the photocurrents and electrochemical impedance. As shown in Fig. 6b, the photocurrent of CdS/Co₃S₄ is higher than that of CdS/Co₃S₄(P), indicating a more efficient electron-hole separation on the photocatalyst using the Co_3S_4 nanosheets. This could be one of the reasons for the higher H_2 evolution rate on CdS/Co₃S₄ than that on CdS/Co₃S₄(P) (Fig. 7a). The electrochemical
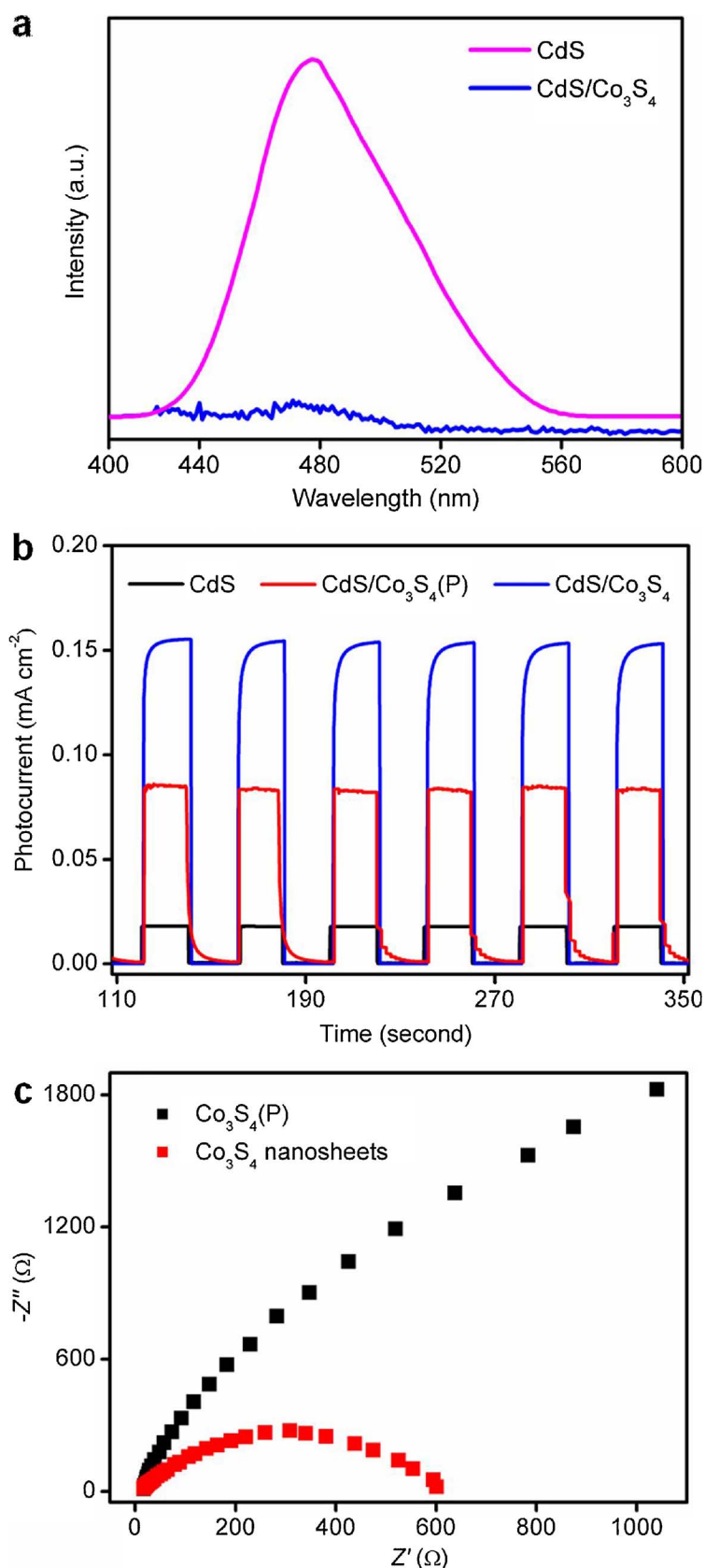
Fig. 6. (a) PL spectra of the pure CdS nanoparticles and CdS/Co$_3$S$_4$ with an excitation wavelength of 365 nm. (b) Transient photocurrent response of the pure CdS nanoparticles, CdS/Co$_3$S$_4$(P) and CdS/Co$_3$S$_4$ in 0.2 M Na$_2$SO$_4$ aqueous solution containing 10 vol% lactic acid under visible light irradiation (λ > 420 nm). (c) Electrochemical impedance spectra of Co$_3$S$_4$(P) and Co$_3$S$_4$ nanosheets.

impedance spectra of Co$_3$S$_4$(P) *vs.* Co$_3$S$_4$ nanosheets in Fig. 6c further demonstrate a higher σ_e (or conductivity) of Co$_3$S$_4$ nanosheets flexible for electron transfer, as compared with Co$_3$S$_4$(P). This is beneficial for more efficient separation of the photoinduced electron-hole pairs on the Co$_3$S$_4$ nanosheets.

Secondly, during the photocatalytic reactions, the Co$_3$S$_4$ nanosheets play as cocatalysts providing the active sites for the photocatalytic reactions. This is demonstrated by the zero H$_2$ evolution on the pure CdS
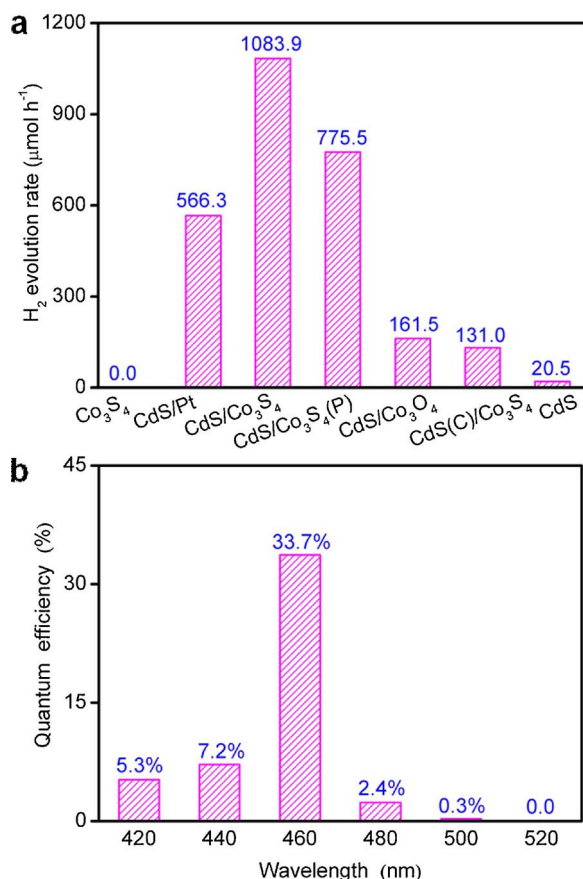
Fig. 7. (a) H_2 evolution rates on the pure Co_3S_4, CdS/Pt, CdS/Co_3S_4, CdS/Co_3O_4, CdS(C)/Co_3S_4 and pure CdS nanoparticles. (b) QE values for CdS/Co_3S_4 at wavelengths of 420, 440, 460, 480, 500 and 520 nm, respectively. Reaction conditions: 100 mL aqueous solution with 10 vol% lactic acid as a hole scavenger, 100 mg photocatalayst, 300 W Xe-lamp (λ > 420 nm).
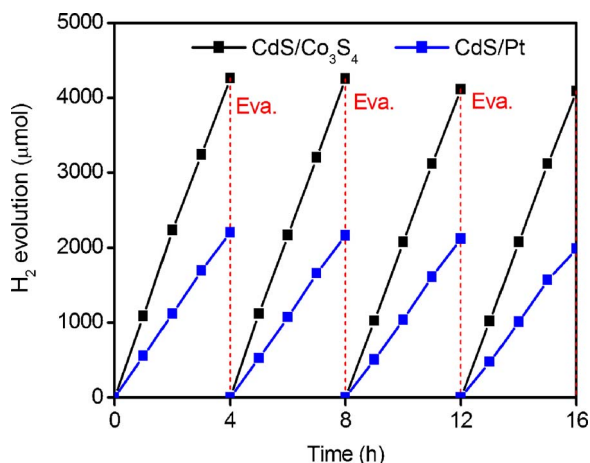

Fig. 8. Stability of CdS/Pt and CdS/Co_3S_4 in the visible-light-driven photocatalytic H_2 evolution from H_2O. Reaction conditions: 100 mL aqueous solution with 10 vol% lactic acid as a hole scavenger, 100 mg photocatalayst, 300 W Xe-lamp (λ > 420 nm).

nanoparticles (Fig. 7a). It has been reported that 2D materials have more surface defects and low-coordinated atoms, which are catalytically active sites, than nanoparticles [6–12]. This could also make some contributions to the higher H_2 evolution rate on CdS/Co_3S_4 than that on CdS/Co_3S_4(P) (Fig. 7a). Thirdly, the Co_3S_4 nanosheet plays as a support for the CdS nanopsrticles, and suppresses the aggregation of the CdS nanoparticles. The Co_3S_4 nanosheets exhibit a positive Zeta potential of about + 47.5 mV. As such, one drive to combine the CdS nanoparticles
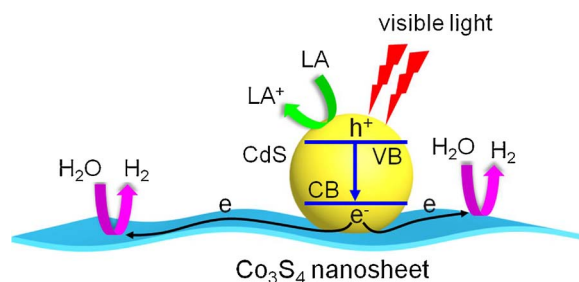

Fig. 9. Possible mechanism of the visible-light-driven photocatalytic H_2 production from H_2O containing lactic acid (LA) as a hole scavenger on CdS/Co_3S_4. CB and VB represent the conduction band and valence band of the CdS nanoparticles, respectively.

(Zeta potential: −36.2 mV) with the Co_3S_4 nanosheets could be the electrostatic interaction. The binding interaction between the Co atoms of Co_3S_4 and the S atoms of CdS as well as the binding interaction between the Cd atoms of CdS and the S atoms of Co_3S_4, as reflected by XPS results (Fig. 5), could also make great contributions to the combination of the CdS nanoparticles with the Co_3S_4 nanosheets. In addition, the higher surface area of the Co_3S_4 nanosheets (62.8 $m^2 g^{-1}$) than that of the Co_3S_4 nanoparticles (32.1 $m^2 g^{-1}$) may also be benefit for the improved H_2 evolution on CdS/Co_3S_4 (Fig. 7a). It is the multiple roles of the Co_3S_4 nanosheets that lead to the enhanced photocatalytic performance on CdS/Co_3S_4.

A possible mechanism for the H_2 evolution from the visible-light-driven photocatalytic H_2O splitting on CdS/Co_3S_4 is proposed in Fig. 9. Visible light absorption by the CdS nanoparticles generates electron-hole pairs. The photogenerated electron-hole pairs are then separated, followed by transfer of the electrons from the CdS nanoparticles to the Co_3S_4 nanosheets. Finally, H_2O is split in the presence of the photogenerated electrons on the Co_3S_4 nanosheets, producing H_2. The photogenerated holes are consumed by the lactic acid molecules which are efficient scavengers of the holes.

4. Conclusions

In summary, a highly efficient H_2 evolution, with a rate of 1083.9 $\mu mol\,h^{-1}$ and a QE of 33.7%, from the visible-light-driven photocatalytic H_2O splitting is achieved on a noble-metal-free CdS/Co_3S_4 photocatalyst fabricated by loading CdS nanoparticles ($\sim$5 nm) on 10-nm-thick 2D Co_3S_4 nanosheets. The photocatalytic H_2 evolution on CdS/Co_3S_4 is significantly enhanced, as compared with those on the Co_3S_4-nanoparticle-based photocatalyst (775.5 $\mu mol\,h^{-1}$) and the noble-metal-based CdS/Pt photocatalyst (566.3 $\mu mol\,h^{-1}$). In the photocatalytic reactions, the Co_3S_4 nanosheets promote the separation of the photogenerated electron-hole pairs, provide catalytically active sites, suppress the aggregation of the CdS nanoparticles which act as light absorbers, thus resulting in the enhanced photocatalytic performance. It is believed that the results of the present work are helpful for designing and fabricating noble-metal-free photocatalysts with higher flexibility for the separation/transfer of the photogenerated charge carriers for achieving more efficient photocatalysis.

Appendix A. Supplementary data

Supplementary data associated with this article can be found, in the online version, at https://doi.org/10.1016/j.apcatb.2017.12.046.

References

[1] J. Low, J. Yu, M. Jaroniec, S. Wageh, A.A. Al-Ghamdi, Adv. Mater. 29 (2017), http://dx.doi.org/10.1002/adma.201601694.

[2] G. Zhang, Z.A. Lan, X. Wang, Angew. Chem. Int. Ed. 55 (2016) 15712–15727.

[3] C. Han, N. Zhang, Y.J. Xu, Nano Today 11 (2016) 351–372.

[4] C. Li, Y. Xu, W. Tu, G. Chen, R. Xu, Green Chem. 19 (2017) 882–899.

[5] Z.F. Huang, J. Song, L. Pan, X. Zhang, L. Wang, J.J. Zou, Adv. Mater. 27 (2015) 5309–5327.

[6] L. Wu, S.Y. Chen, F.J. Fan, T.T. Zhuang, C.M. Dai, S.H. Yu, J. Am. Chem. Soc. 138 (2016) 5576–5584.

[7] T.T. Zhuang, Y. Liu, Y. Li, Y. Zhao, L. Wu, J. Jiang, S.H. Yu, Angew. Chem. Int. Ed. 55 (2016) 6396–6400.

[8] T.T. Zhuang, Y. Liu, M. Sun, S.L. Jiang, M.W. Zhang, X.C. Wang, Q. Zhang, J. Jiang, S.H. Yu, Angew. Chem. Int. Ed. 54 (2015) 11495–11500.

[9] Z.F. Huang, J. Song, L. Pan, Z. Wang, X. Zhang, J.J. Zou, W. Mi, X. Zhang, L. Wang, Nano Energy 12 (2015) 646–656.

[10] J. Di, J. Xia, H. Li, Z. Liu, Nano Energy 35 (2017) 79–91.

[11] W. Yang, X. Zhang, Y. Xie, Nano Today 11 (2016) 793–816.

[12] B. Luo, G. Liu, L. Wang, Nanoscale 8 (2016) 6904–6920.

[13] J. Zhang, Y. Chen, X. Wang, Energy Environ. Sci. 8 (2015) 3092–3108.

[14] S. Zhu, S. Liang, J. Bi, M. Liu, L. Zhou, L. Wu, X. Wang, Green Chem. 18 (2016) 1355–1363.

[15] L. Ye, H. Wang, X. Jin, Y. Su, D. Wang, H. Xie, X. Liu, X. Liu, Sol. Energy Mater. Sol. Cells 144 (2016) 732–739.

[16] F. Lei, Y. Sun, K. Liu, S. Gao, L. Liang, B. Pan, Y. Xie, J. Am. Chem. Soc. 136 (2014) 6826–6829.

[17] A. Boulesbaa, K. Wang, M. Mahjouri-Samani, M. Tian, A.A. Puretzky, I. Ivanov, C.M. Rouleau, K. Xiao, B.G. Sumpter, D.B. Geohegan, J. Am. Chem. Soc. 138 (2016) 14713–14719.

[18] J. Hu, Z. Guo, P.E. Mcwilliams, J.E. Darges, D.L. Druffel, A.M. Moran, S.C. Warren, Nano Lett. 16 (2015) 74–79.

[19] Z. Yu, J. Meng, J. Xiao, Y. Li, Y. Li, Inter. J. Hydrogen Energy 39 (2014) 15387–15393.

[20] M. Zheng, Y. Ding, L. Yu, X. Du, Y. Zhao, Adv. Funct. Mater. 27 (2017) 1605846.

[21] B. Qiu, Q. Zhu, M. Du, L. Fan, M. Xing, J. Zhang, Angew. Chem. Int. Ed. 129 (2017) 2728–2732.

[22] S. Peng, L. Li, S.G. Mhaisalkar, M. Srinivasan, S. Ramakrishna, Q. Yan, ChemSusChem 7 (2014) 2212–2220.

[23] S. Kong, Z. Jin, H. Liu, Y. Wang, J. Phys. Chem. C 118 (2014) 25355–25364.

[24] Y.-X. Pan, J.B. Peng, S. Xin, Y. You, Y.L. Men, F. Zhang, M.Y. Duan, Y. Cui, Z.Q. Sun, J. Song, ACS Sus. Chem. Eng. (2017) 5449–5456.

[25] Y.-X. Pan, H. Zhuang, J. Hong, Z. Fang, H. Liu, B. Liu, Y. Huang, R. Xu, ChemSusChem 7 (2014) 2537–2544.

[26] Z. Fang, Y. Wang, J. Song, Y. Sun, J. Zhou, R. Xu, H. Duan, Nanoscale 5 (2013) 9830–9838.

[27] D.W. Zha, L.F. Li, Y.X. Pan, J.-B. He, Inter. J. Hydrogen Energy 41 (2016) 17370–17379.

[28] Y.-X. Pan, T. Zhou, J. Han, J. Hong, Y. Wang, W. Zhang, R. Xu, Catal. Sci. Technol. 6 (2016) 2206–2213.

[29] H. Wang, Z. Li, G. Li, F. Peng, H. Yu, Catal. Today 245 (2015) 74–78.

[30] Y. Pan, Y. Liu, C. Liu, Appl. Surf. Sci. 357 (2015) 1133–1140.

[31] M. Liu, Y. Fu, H. Ma, T. Wang, C. Guan, K. Hu, Electrochim. Acta 191 (2016) 916–922.

[32] J.G. Terlingen, J. Feijen, A.S. Hoffman, J. Colloid Interface Sci. 155 (1993) 55–65.

[33] X.R. Yu, F. Liu, Z.-Y. Wang, Y. Chen, J. Electron. Spectrosc. Relat. Phenom. 50 (1990) 159–166.

[34] C. O'Sullivan, R.D. Gunning, A. Sanyal, C.A. Barrett, H. Geaney, F.R. Laffir, S. Ahmed, K.M. Ryan, J. Am. Chem. Soc. 131 (2009) 12250–12257.

[35] S.R. Lingampalli, U.K. Gautam, C.N.R. Rao, Energy Environ. Sci. 6 (2013) 3589–3594.

[36] X. Wang, L. Yin, G. Liu, L. Wang, R. Saito, G.Q. Lu, H.M. Cheng, Energy Environ. Sci. 4 (2011) 3976–3979.

[37] J.S. Jang, S.H. Choi, H.G. Kim, J.S. Lee, J. Phys. Chem. C 112 (2008) 17200–17205.

[38] D. Barpuzary, Z. Khan, N. Vinothkumar, M. De, M. Qureshi, J. Phys. Chem. C 116 (2012) 150–156.

[39] R. Marschall, L. Wang, Catal. Today 225 (2014) 111–135.

[40] H. Park, W. Choi, M.R. Hoffmann, J. Mater. Chem. 18 (2008) 2379–2385.

[41] X. Wang, G. Liu, Z.G. Chen, F. Li, L. Wang, G.Q. Lu, H.M. Cheng, Chem. Commun. (2009) 3452–3454.